





Orifice whistling suppression with slow sound

Richard Martin¹ , Khushboo Pandey¹ , Bruno Schuermans¹  and Nicolas Noiray¹ 

¹CAPS Laboratory, Department of Mechanical and Process Engineering, ETH Zürich, Zürich, Switzerland

Corresponding author: Nicolas Noiray, noirayn@ethz.ch

(Received 29 November 2024; revised 31 May 2025; accepted 16 July 2025)

When a low Mach flow is imposed through an orifice at the end of a cavity, intense whistling can occur. It results from the constructive feedback loop between the acoustic field of the cavity and coherent vortex shedding at the edges of the orifice with bias flow. Whistling is often a source of unwanted noise, demanding passive control strategies. In this study, it is shown that whistling can be suppressed by utilising the slow-sound effect. This periodic arrangement of small cavities detunes the cavity from the frequency range where the orifice flow exhibits a potential for acoustic energy amplification, by reducing the effective speed of sound inside the cavity. Acoustic and optical measurement techniques are employed, including scattering matrix and impedance measurements, and particle image velocimetry to reconstruct the velocity field downstream of the orifice. The production and dissipation of acoustic energy is investigated using Howe's energy corollary. The spatio-temporal patterns of the vortex sound downstream of the orifice are revealed. They are deduced from phase-averaged acoustic and Lamb vector fields and give qualitative insight into the physical mechanisms of the whistling phenomenon.

Key words: aeroacoustics, instability control, jets

1. Introduction

Environmental noise is ubiquitous in the everyday life of humans. It originates from many anthropogenic sources, like road, rail and air traffic, and industrial sites, for example. Even though noise is normally considered just a nuisance, continuous exposure to it can have severe effects on human health causing, amongst others, cardiovascular diseases, sleep disturbance and cognitive impairment. The World Health Organisation estimates that due to environmental noise every year up to one million healthy life years are lost in Western Europe (Theakston 2011). Tonal noise, that is noise with a dominant narrow-banded

frequency peak, can be particularly disturbing if it is high pitched (Radosz 2021). This form of noise can for instance originate from rotating machinery, from high Mach cavity flows or from low Mach aeroacoustic sources which constructively interact with an eigenmode of a cavity. The latter type of whistling can be categorised as a self-oscillation, where a steady source of energy in the form of a moving fluid causes coherent pressure and velocity oscillations which can be perceived as audible sound. Besides potentially contributing to environmental noise, whistling can also cause problems in technical applications. One example is the high-frequency whistling noise in the injectors of a representative rocket engine which couples to thermoacoustic oscillations in the combustion chamber, as reported by Armbruster, Hardi & Oschwald (2022). Cases like this motivate research to avoid or mitigate the occurrence of this type of tonal noise.

One early example of a scientific study on whistling is the work by Sondhauss (1854), who investigated the sound produced by differently shaped orifices subject to bias flow. This phenomenon was further studied by Strutt (1945), who considered a simple set-up comprising a resonating tube, terminated by a plate with an aperture on one side and an open end on the other side. A flow through the aperture in either direction caused audible whistling tones. Extensive studies on a system like this were conducted by Anderson (1952, 1955). He called the resulting whistling sounds pipe tones or *Pfeifentöne*. A comprehensive review on various whistling mechanisms and whistling research can be found in Blake & Powell (1986) and the reader can also refer to the work of Brandão & Schnitzer (2020). More recently, the mechanism of orifice whistling was studied by Testud *et al.* (2009) and Kierkegaard *et al.* (2012), who investigated the whistling potentiality of orifices in a flow duct and self-excited systems comprising an orifice and resonating ducts of different lengths. Yang & Morgans (2016, 2017) derived semi-analytical models for the aeroacoustic system of the shear layer, which was later revisited by Brokof *et al.* (2023) with a numerical model based on the linearised Navier–Stokes equations (LNSE). The incompressible LNSE were used by Sierra-Ausin *et al.* (2022) to determine the impedance of a circular hole with bias flow, and to predict the stability of the system with and without a tuned resonator. Furthermore, in the works of Ma, Slaboch & Morris (2009) and Zhang & Bodony (2012), the whistling of cavities whose orifice is subject to a grazing flow is respectively investigated with numerical simulations and experiments.

This paper focuses on the whistling obtained with a flow through an orifice placed upstream of an acoustic longitudinal cavity. The whistling occurrence depends on the thickness of the orifice plate, the jet velocity and the cavity geometry. Whistling can occur in both cases, when the cavity is placed upstream, or downstream of the orifice (Strutt 1945). Figure 1 shows Mie scattering images of two jets with the same Reynolds number. In figure 1(a) the system is whistling, because an appropriately tuned resonating cavity is placed downstream of the orifice. At the orifice, vortices are shed in regular intervals coherent with the acoustic pressure oscillations. If the system is whistling, sound produced by the shed vorticity of the jet is amplified by the acoustic cavity, causing strong pressure oscillations close to the orifice. These pressure oscillations modulate the velocity fluctuations in the flow direction. This periodic forcing of the jet causes even stronger fluctuations in the vorticity and thus more sound production by the vortices. Eventually, a limit cycle is reached where the sound production is in equilibrium with the acoustic losses of the system. The system in figure 1(b) is not whistling, because the cavity was detuned, such that the acoustic resonance frequencies are not close enough to the frequency of the hydrodynamic modes of the jet.

The mechanism of how sound is produced by travelling vortices is described by Howe's vortex sound theory (Howe 1975, 1980). It expresses how the rotational (solenoidal) velocity field interacts with the acoustic velocity field to produce or dissipate

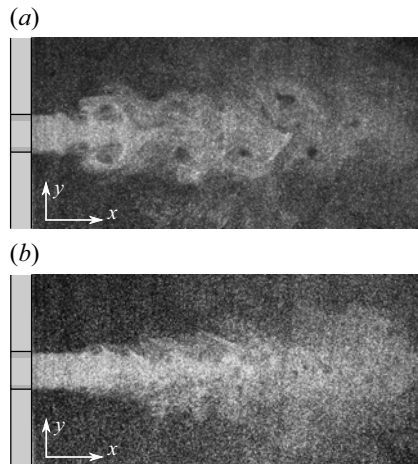


Figure 1. Mie scattering images of two jets with the same Reynolds number: (a) whistling due to coherent vortex shedding, (b) not whistling. Movies can be seen in supplementary material.

acoustic energy. Using Howe's vortex sound theory, the whistling of apertures, small gaps and cavities was already investigated in many studies. Bruggeman *et al.* (1991) investigated the whistling of a side branch of a duct, subject to grazing flow. A similar system is the whistling of a beer bottle, which was studied by Boujo *et al.* (2020). They used particle image velocimetry (PIV) to obtain the rotational velocity field experimentally and a finite element simulation to obtain the irrotational velocity field. Matsuura & Nakano (2012) investigated the whistling noise of a hole tone using direct numerical simulation and calculated the vortex sound production by decomposing the velocity field into a rotational and an irrotational part using a Helmholtz–Hodge decomposition. They found that the maximum of the instantaneous acoustic power production occurs close to the leading edge of the hole. Unnikrishnan & Gaitonde (2016) investigated the sound emitted from a supersonic cold jet in terms of the total fluctuating enthalpy using large eddy simulation. Besides these canonical examples of sound production, the vortex sound theory was also applied by Lee *et al.* (2022) to the case of whistling of a narrow gap of an automobile side mirror. To the knowledge of the authors, the vortex sound theory has not been applied to experimental data of bias flow orifice whistling or pipe tones.

Orifice whistling has been found to be effectively mitigated by changing either the hydrodynamic stability of the jet or by detuning the acoustic cavity. The effect of different orifice geometries on the whistling frequency was investigated by Testud *et al.* (2009). Guzmán-Iñigo & Morgans (2024) optimised the trailing edge of a bevelled orifice to change the system's propensity to whistling. Kierkegaard *et al.* (2012) changed the lengths of the acoustic cavities upstream and downstream of the orifice. They found that certain combinations of cavity lengths are less prone to cause whistling than others.

Changing the geometry of a cavity as done by Kierkegaard *et al.* (2012) is one way to change its eigenfrequency. Alternatively, the properties of the acoustic medium can be changed. For example, an increase in temperature also increases the speed of sound and therefore the eigenfrequency of a cavity (Miniero *et al.* 2023). However, to achieve large differences in the speed of sound, a very large temperature difference would be needed, which would be impractical for many applications. Instead, the effective speed of sound can be reduced by adding an array of high-frequency small cavities to the main resonating cavity. The addition of these small cavities increases the acoustic compliance of the

cavity sidewall, already in the low-frequency limit $f \rightarrow 0$. This effect is also observed in corrugated pipes, where the additional volume of the non-resonating corrugation decreases the effective speed of sound in the longitudinal direction of the pipe (Russo *et al.* 2016). The approach of changing the effective material properties of the black-box system is commonly referred to as acoustic metamaterials (Cummer, Christensen & Alù 2016), although in this paper, the aforementioned phenomenon is simply called the slow-sound effect. The dispersion of acoustic waves in Helmholtz resonator arrays was studied by Sugimoto & Horioka (1995) and Aurégan & Pagneux (2015), for example. While in the low-frequency limit, these structures are known to reduce the effective speed of sound, close to the eigenfrequency of the sidewall small cavities, the effective speed of sound in axial direction vanishes, creating a stop band for acoustic wave propagation.

In this paper, orifice whistling is suppressed by detuning the acoustic cavity using the slow-sound effect in its low-frequency limit. The geometries of the tuned and the detuned cavities and their design is presented in § 2, followed by the experimental set-up in § 3. The experimental results are shown in § 4. The pressure fluctuations of the system arising from the self-excited oscillations are investigated for various flow rates. Particle image velocimetry measurements of the flow downstream of the orifice show coherent vortex shedding for the tuned resonating deep cavity and the absence of it for a cavity of the same length, but with the slow-sound effect. Howe's energy corollary is applied to study the whistling mechanism. For this purpose, a finite element model of the Helmholtz equation is used to determine the irrotational part of the velocity fluctuations.

2. Slow-sound-based cavity detuning

In this section, the principle of the slow-sound-based cavity whistling suppression is presented. Figure 2 shows a schematic of the two geometries considered in this work; the reference cavity REC and the slow-sound cavity SSC, respectively depicted in figures 2(a) and 2(b). Both cavities consist of a duct terminated by an orifice plate on the upstream side and open to an infinite volume on the downstream side. These cavities are subject to a mass flow \dot{m} in the positive x -direction. The airflow is supplied from a pipe upstream of the orifice plate. At the orifice, flow separation occurs and a cylindrical shear layer forms. This shear layer can amplify or attenuate incident acoustic waves. In both cavities acoustic waves propagate with the speed of sound c . The standard wavenumber is $k = \omega/c$. The mean density of the medium is ρ . The waves travelling in the positive x -direction are characterised by the Riemann invariant F , and the waves travelling in the negative x -direction are characterised by G . In the upstream pipe, waves are not reflected by the far upstream end ($F_u \rightarrow 0$). In the main cavities, the large area expansion at the downstream end causes a significant reflection of acoustic waves. Therefore, they can be regarded as approximate quarter-wave resonators. The orifice shape and the overall lengths and cross-sectional areas of the cavities are the same for both devices REC and SSC.

The SSC differs from the REC as a periodic arrangement of small cavities is connected to one of the cavity sidewalls. This array of sidewall small cavities makes the wall acoustically compliant. As a result, the wavenumbers in k_y and k_z are complex and the wave propagation in the axial direction with the wavenumber k_x changes. This relationship is expressed by the compatibility relation of modes in a rectangular duct $k^2 = k_x^2 + k_y^2 + k_z^2$ (Munjal 2014). For the low-frequency limit, the ratio of the axial wavenumber to the standard wavenumber is $k_x/k = \sqrt{1 + \sum V_r/V_c}$, where $\sum V_r$ is the combined volume of all small cavities and V_c is the volume of the main deep cavity they are attached to (Sugimoto & Horioka 1995; Russo *et al.* 2016). A derivation of this equation for the geometry presented in this paper can be found in Appendix A. For a finite small cavity

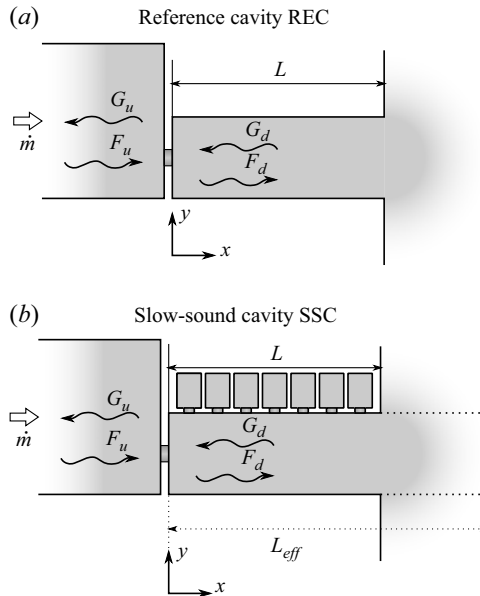


Figure 2. Sketches of the reference cavity (a, REC) and slow-sound cavity (b, SSC). Both cavities of length L are connected to an upstream duct through an orifice plate on the upstream side and open to an infinite volume on the downstream side. A bias flow \dot{m} is imposed for both cavities through their upstream orifice. The dotted lines in (b) illustrate a cavity of length L_{eff} without the slow-sound effect that has the same resonance frequency as the SSC.

size V_r , the axial wavenumber k_x is larger than k . This can be interpreted as a reduction in the effective speed of sound in this channel $c_{eff} < c$. This slow-sound effect can be used to detune the approximate quarter-wave resonator, whose resonance condition is obtained for when $\cot(k_x L) \rightarrow 0$, where L is the length of the deep cavity (Munjal 2014). Conceptually, increasing k_x has the same effect as increasing L . This is illustrated in figure 2(b) with a non-slow-sound cavity of length L_{eff} which could be used to replace the SSC. The effect of the resonator length L on the whistling of an orifice was investigated by Kierkegaard *et al.* (2012). They found that changing the lengths of resonating ducts upstream and downstream of the orifice can lead to cases where the system does not whistle.

Figure 3 shows the geometries of the additively manufactured elements to be inserted in a duct to form the REC and the SSC. Both elements are symmetric with respect to a plane defined by $0 = y - z$ going through the centre of the orifice at $(x, y, z) = (0, 0, 0)$. The REC and SEC elements are mounted inside a large duct with a cross-section of $62 \times 62 \text{ mm}^2$ which has quartz glass windows for optical access inside the cavity. The overall length is 150 mm, with a 3.2 mm thick orifice and a cavity of length $L = 146.8 \text{ mm}$. The cross-section of the cavities is $30 \times 30 \text{ mm}^2$. They occupy approximately a quarter of the cross-section of the large duct and are placed in the bottom left corner of the large duct. When the elements are mounted in the duct, the two open sides of the cavity are closed by the windows of the large duct, enabling optical access. The orifice, depicted in figure 3(c), has sharp edges and a diameter of $D = 6.6 \text{ mm}$. The SSC element, depicted in figure 3(b), has a total of 20 sidewall small cavities, 10 in the x direction with one each in the y - and z -directions. Each small cavity has the shape of a prism with an approximate right trapezium as a base. The volume of one small cavity is $V_r \approx 7500 \text{ mm}^3$. The corresponding factor for the detuning in the low-frequency limit is accordingly $k_x/k = 1.46$. Therefore,

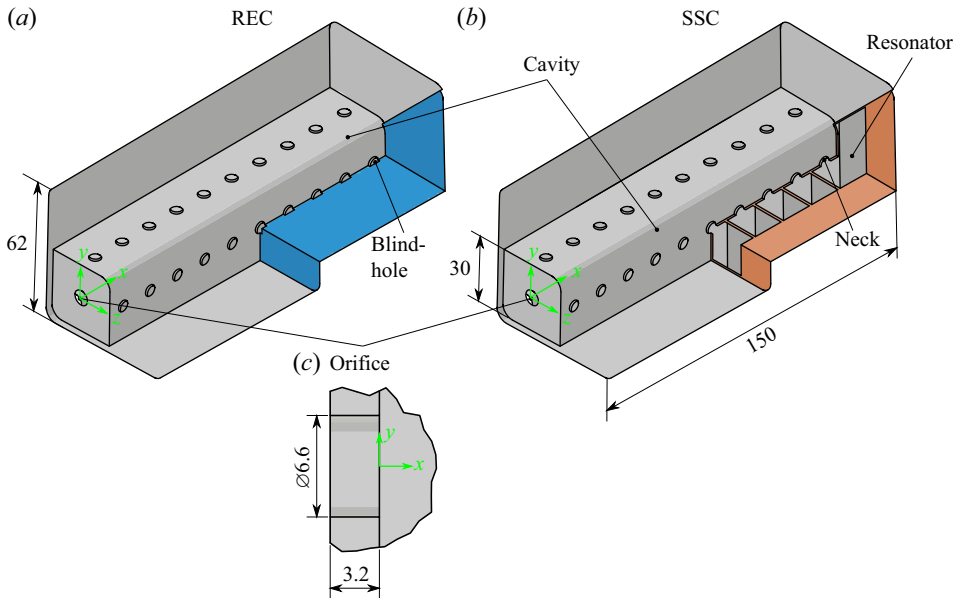


Figure 3. Cutaway drawings of the additively manufactured elements to be inserted in the duct to form the REC and the SSC, cut surfaces are shown in colour, cavity surface is concave; (a) element forming the reference cavity (REC), (b) element forming the slow-sound cavity (SSC), (c) detail of the orifice geometry.

sound propagates inside the main deep cavity in the x -direction with an effective speed of $c_{eff} = 0.68c$ and its resonances are shifted to lower frequencies.

The small cavities are connected to the duct with necks which have a diameter of 5 mm and a length of 1 mm. The resonance frequency of the small cavities can be estimated by using the formula for the resonance of a Helmholtz resonator, which is (Munjal 2014)

$$f_{res} = \frac{c}{2\pi} \sqrt{\frac{a_n}{l_{n,eff} V_r}}, \quad (2.1)$$

where a_n is the cross-sectional area of the neck and $l_{n,eff} = l_n + 1.7$ is the effective length of the neck. Using this equation, the resonance frequency of the small cavities is estimated to be $f_{c,res} = 1.2$ kHz, which is approximately twice as high as the whistling frequency, which is expected at the first longitudinal resonance of the cavity downstream of the orifice, which can be approximated by a quarter-wave resonator with a frequency of $f = c/(4L) \approx 600$ Hz. Thus, the sidewall small cavities are not dissipating a significant amount of acoustic energy at the whistling frequency. The main effect on the system is the detuning via the slow-sound effect in the low-frequency limit. The REC element depicted in figure 3(a) has 20 blind holes at the same position and with the same dimensions as the SSC element. This aims to reduce differences in the flow close to the wall between the REC and the SSC.

3. Experimental set-up

In this section, the experimental set-up for the acoustic measurements and the optical measurements is presented. All experiments were conducted at room temperature and atmospheric pressure (table 1). Three different types of experimental set-ups were used to study the whistling cavities. The properties of the orifice were obtained using scattering matrix measurements. The acoustic properties of the REC and SSC were studied

Property	Symbol	Value	Property	Symbol	Value
Speed of sound	c	343 m s^{-1}	Orifice thickness	t_{or}	3.2 mm
Ambient temp.	T	$21 \pm 1 \text{ }^{\circ}\text{C}$	Deep cavity length	L	146.8 mm
Ambient pressure	\bar{p}	970 hPa	Whistling frequency	f	661 Hz
Density	ρ	1.15 kg m^{-3}	Mach number	$Ma = U/c$	2.2×10^{-2}
Dynamic viscosity	μ	$1.82 \times 10^{-5} \text{ Pa s}$	Reynolds number	$Re = \rho U D / \mu$	3180
Bulk velocity	U	7.6 m s^{-1}	Strouhal number	$St = f t_{or} / U$	0.27
Orifice diameter	D	6.6 mm	Helmholtz number	$He_L = f L / c$	0.28

Table 1. Properties of the acoustic medium during the experiments and dimensionless quantities for the whistling REC at $\dot{m} = 0.3 \text{ g s}^{-1}$.

using acoustic impedance measurements. The whistling conditions, i.e. self-sustaining aeroacoustic oscillations, were studied using PIV. For all experiments with flow, a mass flow \dot{m} of air originating from a pressurised shop-air line is controlled with a Bronkhorst thermal mass flow controller and injected into the upstream near-anechoic end.

The acoustic properties of the orifice subject to bias flow were determined in the same fashion as in Testud *et al.* (2009), using an orifice with the same dimensions as in figure 3(c) in an aluminium plate placed in the middle of the $62 \times 62 \text{ mm}^2$ duct (waveguide) in the absence of the resonating cavity. The system was forced first from the upstream and later from the downstream side with sinusoidal waves using compression drivers. The forcing frequency was varied from $f = 250$ to $f = 2500 \text{ Hz}$ in steps of 5 Hz . The Riemann invariants upstream and downstream of this orifice plate were reconstructed using the multiple microphone method (Jang & Ih 1998) with four microphones distributed along the ducts on either side of the orifice. The test was repeated for mass flow rates in the range of $0\text{--}0.6 \text{ g s}^{-1}$, in steps of 0.2 g s^{-1} .

The admittances from the upstream side of the REC and SSC were measured using an impedance tube arrangement with four microphones mounted to the waveguiding duct. The system was forced from the upstream side using a compression driver at the same frequencies as for the scattering matrix measurements. On the downstream side, the cavities were mounted flush to the flange of the duct. To avoid whistling, the system was studied without a mass flow $\dot{m} = 0$.

The set-up for the PIV measurements under flow conditions is depicted in figure 4. It is conceptionally similar to Kierkegaard *et al.* (2012). The main components are a flow duct, terminated by a near-anechoic end on the upstream side at $x = -393 \text{ mm}$, and an open end with a flange on the downstream side at $x = 146.8 \text{ mm}$. The REC and SSC elements from figure 3 are placed flush to the downstream flange. With the chosen system of coordinates, the trailing edge of the orifice is at $x = 0 \text{ mm}$, and its centreline is at $(y, z) = (0, 0) \text{ mm}$. One microphone is mounted flush to the duct wall on the upstream side of the cavity at $(x, y, z) = (-68, 47, 16) \text{ mm}$. Two quartz glass windows for optical access are installed in the duct at the section with the cavity. For the self-excited tests, the pressure fluctuations at the microphone are recorded at mass flow rates between $\dot{m} = 0.2$ and $\dot{m} = 0.6 \text{ g s}^{-1}$ in steps of 0.01 g s^{-1} . At each step, the acoustic data are recorded for a duration of 1 s at a sampling rate of 50 kHz .

For a mass flow rate of $\dot{m} = 0.3 \text{ g s}^{-1}$, the REC whistles, and the corresponding flow field, as well as the one for the SSC at the same mass flow rate, are studied using PIV. For this purpose, the flow is seeded with di-ethyl-hexyl-sebacat. The PIV set-up is depicted in figure 4 cut A – A. It comprises a Photonics Industries DM Series pulsed laser in single-exposure double-frame mode with a time difference of $\Delta t = 10 \text{ } \mu\text{s}$ between the

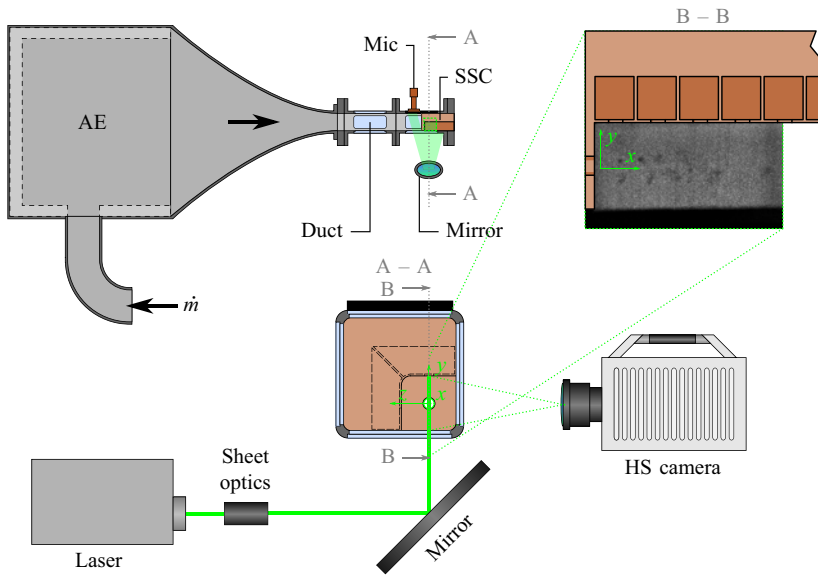


Figure 4. Experimental set-up (not to scale) in the absence of acoustic forcing using loudspeakers. Test section with near-anechoic end (AE), microphone (mic), duct ($62 \times 62 \text{ mm}^2$) with or without flow which acts as an acoustic waveguide, PIV set-up comprising laser, sheet optics, mirror, high-speed (HS) camera. The REC and SSC (here in orange) are formed by the additively manufactured elements inserted at the downstream end of the duct.

laser pulses. A laser sheet is created using sheet optics and a mirror deflects it into the test section. The laser sheet illuminates the (x, y) -plane at the centre of the orifice $z = 0$. A Photron Fastcam SA-X2 high-speed camera records the illuminated plane at a frame rate of 6 kHz for a duration of 454.5 ms. The image and audio recordings are triggered simultaneously by an external source. The settings for the audio recordings are the same as before. The field of view of the camera is depicted in [figure 4](#) cut B – B.

4. Results

In this section, the results of the acoustic tests and the optical measurements using PIV for the orifice, as well as for the REC and SSC, are presented. The section concludes with a discussion of the vortex sound after Howe (1975), which was calculated for the case of the whistling REC at a mass flow rate of 0.3 g s^{-1} using a hybrid approach utilising a finite element model to estimate the acoustic velocity field.

4.1. Acoustic measurements

Three experiments are conducted to study the acoustic properties of the orifice and the REC and SSC. The results are presented in this subsection. First, the results of the scattering matrix measurements of the orifice for various flow rates are used to calculate the whistling potentiality after Testud *et al.* (2009). Afterwards, the admittances of the upstream interface of the two cavities are presented, showing the resonances of the systems. Finally, the acoustic radiation from the self-excited cavities is compared for various flow rates. Relevant dimensionless quantities determined for the whistling case are tabulated in [table 1](#).

Any acoustic system can be regarded as a multi-port system, with waves entering and leaving the system through the ports. In the case of a one-dimensional system with two

ports, the scattering matrix S expresses the relation between the incident waves F_u and G_d to the scattered waves F_d and G_u (Testud *et al.* 2009)

$$\begin{bmatrix} G_u \\ F_d \end{bmatrix} = \underbrace{\begin{bmatrix} R^+ & T^- \\ T^+ & R^- \end{bmatrix}}_S \begin{bmatrix} F_u \\ G_d \end{bmatrix}, \quad (4.1)$$

where R^\pm are the reflection coefficients and T^\pm are the transmission coefficients in positive (+) and negative (−) directions, respectively. The scattering matrix S characterises the behaviour of the acoustic two-port system fully. In the case of the orifice, the elements of the matrix depend on the mass flow rate \dot{m} and the frequency f of the waves. The upper and lower limits of the ratio of dissipated or generated acoustic power can be derived from this matrix (Aurégan & Starobinski 1999). The eigenvalues λ_i of the matrix $S^\dagger S$, where $(\cdot)^\dagger$ denotes the Hermitian transpose, give the maximum possible dissipation ($\lambda_{\min} < 1$ or $\Sigma_{\max} = 1 - \lambda_{\min} > 0$) or the maximum possible amplification or generation ($\lambda_{\max} > 1$ or $\Sigma_{\min} = 1 - \lambda_{\max} < 0$) of acoustic energy. Note, that the potentiality for sound amplification $\Sigma_{\min} < 0$ is a necessary but not a sufficient condition for whistling to occur. To evaluate the system's stability, the zeros of the total impedance of the system have to be considered (Kierkegaard *et al.* 2012; Sierra-Ausin *et al.* 2022).

The interface of an acoustic system can be described by its admittance, which is the reciprocal of the impedance. For this study, the specific acoustic admittance Y on the upstream side of the acoustic devices at $x = -3.2$ mm can be defined as

$$Y = \frac{F_u - G_u}{F_u + G_u} = \frac{\rho c u_{ac}}{p_{ac}}. \quad (4.2)$$

The absolute value of Y quantifies, how large acoustic velocity fluctuations u_{ac} will be at the orifice for an acoustic pressure forcing p_{ac} . At the resonance frequency of the system, the admittance is at a local maximum.

The results of the scattering matrix measurements and the admittance measurements are depicted in figure 5. In figure 5(b) the results for the whistling potentiality after Testud *et al.* (2009) are shown. Here, Σ_{\max} is plotted with dashed red lines and Σ_{\min} is plotted with solid blue lines. The value of Σ_{\min} for $\dot{m} = 0 \text{ g s}^{-1}$ is plotted with a solid black line. Both Σ_{\max} and Σ_{\min} for $\dot{m} = 0.0 \text{ g s}^{-1}$ are positive or very close to zero. Thus, without a mean flow, a comparably small amount of acoustic energy is absorbed by the orifice. For $\dot{m} = 0.2 \text{ g s}^{-1}$ Σ_{\min} has clear local minima smaller than zero below $f = 500$ Hz. With increasing mass flow rate \dot{m} , the local minimum of Σ_{\min} shifts to higher frequencies. Figure 5(c) shows how the local minima of Σ_{\min} collapse, if f is non-dimensionalised using the Strouhal number $St = f t_{or} / U$, where t_{or} is the orifice thickness and U is the average velocity at the orifice (Testud *et al.* 2009). Here, the Strouhal number for the first local minimum is $St \approx 0.25$, which is close to the values reported by Testud *et al.* (2009) for similarly shaped orifices. The strongest possible amplification of acoustic energy ($\min(\Sigma_{\min})$) occurs in the range of mass flow rates between $\dot{m} = 0.3$ and $\dot{m} = 0.4 \text{ g s}^{-1}$ at frequencies between $f = 560$ and $f = 860$ Hz.

Figure 5(a) shows the absolute value of the admittance $|Y|$ in the absence of flow. It can be seen that the reference cavity REC has a local maximum at $f_{REC, res} = 665$ Hz, which corresponds approximately to the quarter-wave resonance of the REC, i.e. the Helmholtz number He_L is close to 0.25. This local maximum of the admittance falls in the range where Σ_{\min} in figure 5 has a local minimum below zero for a mass flow rate of $\dot{m} = 0.3 \text{ g s}^{-1}$. Therefore, whistling around this frequency and mass flow rate is expedited, because small fluctuations in pressure can induce large velocity fluctuations, which lead

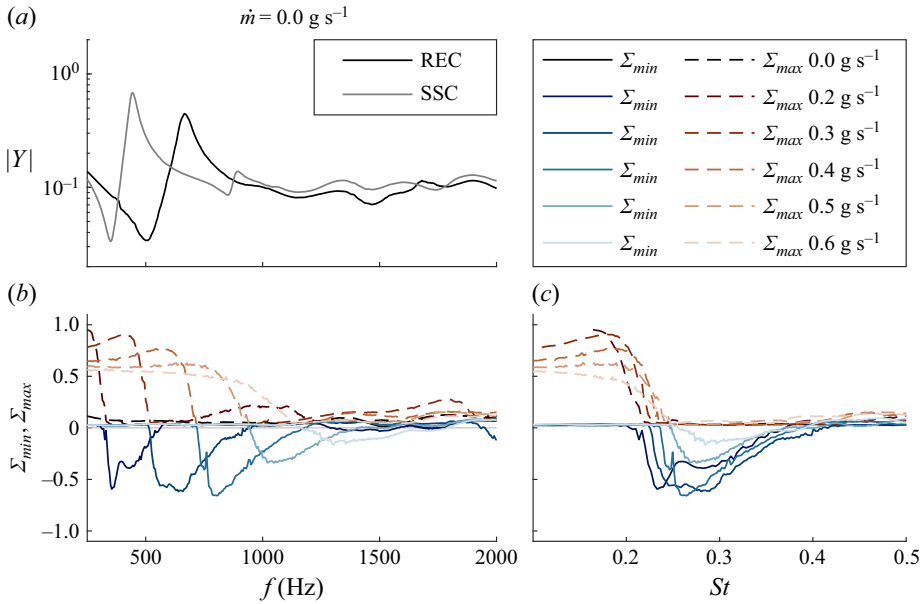


Figure 5. Acoustic measurements with excitation: (a) absolute value of the specific admittance Y on the upstream side of the cavity in the absence of flow, (b) whistling potentiality of the orifice after Testud *et al.* (2009), (c) whistling potentiality depending on Strouhal number St .

to stronger vorticity fluctuations. The admittance of the SSC shows its local maximum at lower frequencies $f_{SSC,res} = 445 \text{ Hz}$, a factor of 1.5 smaller than the reference, which corresponds to the previously discussed ratio of wavenumbers k_x/k . At this frequency, the minimum of Σ_{min} is obtained for $\dot{m} = 0.2 \text{ g s}^{-1}$ and it is still negative. However, the whistling potential is not as strong for $\dot{m} = 0.2 \text{ g s}^{-1}$ at 445 Hz as for $\dot{m} = 0.3 \text{ g s}^{-1}$ at 665 Hz. Furthermore, for $\dot{m} > 0.2 \text{ g s}^{-1}$ Σ_{min} vanishes at the resonance frequency of the SSC. Thus, whistling for $\dot{m} = 0.2 \text{ g s}^{-1}$ can be potentially mitigated in the SSC, by shifting the resonance frequency out of the range of large sound amplification of the orifice. One can also note that the value at the local maximum in the admittance for the SSC is larger than for the REC, which is due to the compliant sidewall of the cavity. This underlines the fact that the main effect of the small cavities in the frequency range of the whistling is a detuning of the cavity rather than a dissipation enhancement. Dissipation plays a larger role close to the resonances of the small cavities at around 1.2 kHz. Around this frequency, there is a stop band in the transmission spectrum of the SSC (Jiménez *et al.* 2017). It is important to note here that the data presented in figure 5(a) were obtained without flow. In the presence of flow, the reflection properties of the orifice change due to the coupling between the aeroacoustic properties of the orifice and the cavity acoustics.

The conjunction of the resonances of the deep cavity with the whistling potentiality of the orifice shows that the REC can potentially whistle at a mass flow rate of $\dot{m} = 0.3 \text{ g s}^{-1}$ with a frequency of around $f = 665 \text{ Hz}$, whereas the SSC is less likely to whistle for this mass flow rate. This notion is verified using the set-up for self-excited oscillations shown in figure 4. Figure 6 shows the results of the self-excited tests. The figure shows the time traces of the pressure oscillations p' upstream of the orifice at the microphone at $x = -68.2 \text{ mm}$, and the power spectral densities depending on the mass flow rate \dot{m} . In figure 6(a) the pressure oscillations p' are shown for a mass flow rate of $\dot{m} = 0.3 \text{ g s}^{-1}$ during a 5 ms interval. For the REC, a clear sinusoidal oscillation with a large amplitude

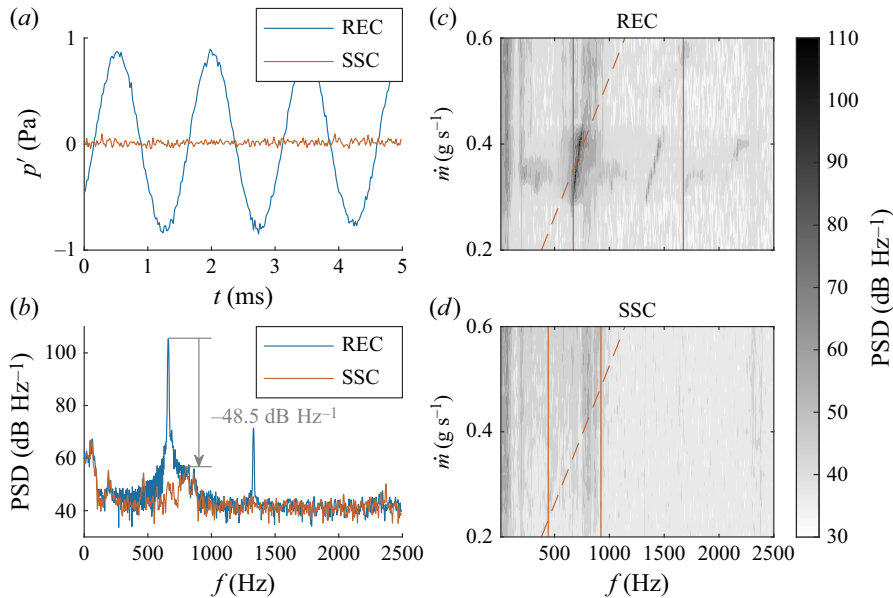


Figure 6. Self-excited measurements: (a) time trace of pressure fluctuations p in the upstream duct at $x = -68.2$ mm for REC and SSC, (b) comparison of power spectral density PSD at $\dot{m} = 0.3 \text{ g s}^{-1}$, (c,d) PSD for various mass flow rates.

can be seen, whereas for the SSC, there are no coherent oscillations visible, only noise with a low power. The sound radiation of both cavities in the upstream waveguide can be compared directly using the sound pressure level $SPL = 20 \log_{10}(p_{rms}/p_0)$, where p_{rms} is the root-mean-squared value of the pressure and $p_0 = 20 \text{ } \mu\text{Pa}$ is the reference pressure (Munjal 2014). The value for the REC is $SPL_{REC} = 90.8 \text{ dB}$, the value for the SSC is significantly lower at $SPL_{SSC} = 64 \text{ dB}$, corresponding to a reduction of 26.8 dB_{SPL} . Thus the whistling is effectively mitigated for this flow rate.

This reduction of the sound emissions can also be seen in the power spectral density (PSD) in figure 6(b). The PSD was calculated from p' using Welch's method with a window 10 000 samples wide and an overlap of 1000 samples. For the REC, a clear peak with a value of 105 dB Hz^{-1} can be seen at $f = 661 \text{ Hz}$, with the first harmonic visible at $f = 1331 \text{ Hz}$. For the SSC, the highest peak in the range of the whistling frequency has a value of 56.5 dB Hz^{-1} and is therefore 48.5 dB Hz^{-1} lower than for the whistling REC. A small peak in the spectrum of the SSC at $f = 466 \text{ Hz}$ indicates the shifted resonance of the SSC. However, this peak does not correspond to an aeroacoustic limit cycle but to the quarter-wave resonance of the SSC driven by broadband noise of the turbulent flow. Note that the noise produced by the injection of the air upstream of the near-anechoic chamber located before the deep cavity (see figure 4) is significantly reduced by acoustic energy absorbing foam of this chamber (see also Bourquard, Faure-Beaulieu & Noiray 2021). This muffled broadband noise forces the deep cavity and the resulting sound level to not exceed 70 dB . The acoustic energy is concentrated at low frequency, below 300 Hz , and its spectral distribution is identical in both REC and SSC.

Figure 6(c,d) shows the PSD for various mass flow rates. The eigenfrequencies were calculated using a finite element simulation of the Helmholtz equations of the system, which is discussed in § 4.3. They are plotted as vertical solid lines. The Strouhal number corresponding to the whistling $St = 0.27$ was obtained from the whistling potentiality in figure 5(c). It is plotted as an oblique dashed line, using $St = f t_{or}/U = 0.27$ and

$U = \dot{m}/(\rho\pi D^2/4) = 7.6 \text{ m s}^{-1}$. For the REC clear streaks corresponding to the whistling frequency and its first harmonic are visible. The fundamental frequency is in the range where the line of the acoustic mode intersects with the line of the Strouhal number of maximum whistling potentiality at $f = 661 \text{ Hz}$ and $\dot{m} = 0.35$. There, the acoustic field is strongly coupled to the hydrodynamic instability of the jet. For the SSC, this intersection of the lines of the shifted acoustic eigenfrequencies with the line of the Strouhal number occurs at lower or higher mass flow rates $\dot{m} = 0.23$ and $\dot{m} = 0.48 \text{ g s}^{-1}$, where the whistling potentiality is much lower (see [figure 5b](#)). Thus, the bias flow in the cavity's orifice does not lead to whistling.

4.2. Optical measurements

In this section, the results of the optical measurements using PIV are presented and the whistling REC is compared with the non-whistling SSC. First, the time-averaged properties of the flow are discussed. Afterwards, the fluctuating component of the vorticity is investigated. The considered mass flow rate is $\dot{m} = 0.3 \text{ g s}^{-1}$ for the REC and the SSC. The high-speed images are post-processed with the PIV algorithm of LaVision DaVis 8, using the multi-pass method with decreasing window size. The reconstructed velocity field consists of $231 \times 101 = 23\,331$ vectors. The corners of the field are at $(x, y) = (1.13, -10.66)$ and $(x, y) = (53.10, 11.93) \text{ mm}$. The vector spacing is 0.226 mm in the x - and y -directions.

For the investigation of the flow, a convenient triple decomposition of the flow variables is chosen (Hussain & Reynolds 1970; Bourquard *et al.* 2021). The total velocity \mathbf{u} of the flow can be decomposed such that

$$\mathbf{u} = \underbrace{\bar{\mathbf{u}}}_{\langle \mathbf{u} \rangle} + \underbrace{\tilde{\mathbf{u}}}_{\mathbf{u}'} + \check{\mathbf{u}}, \quad (4.3)$$

where $\bar{\mathbf{u}}$ denotes the time-averaged velocity, $\langle \mathbf{u} \rangle$ denotes the phase-averaged velocity, of which $\tilde{\mathbf{u}}$ are the coherent velocity fluctuations, and \mathbf{u}' are the velocity fluctuations, including the incoherent fluctuations $\check{\mathbf{u}}$. The phase-averaged velocity fluctuations $\tilde{\mathbf{u}}$ can be further decomposed into the irrotational acoustic velocity field \mathbf{u}_{ac} and a solenoidal velocity field. Other flow variables like the vorticity $\boldsymbol{\omega}$ can be decomposed in the same way.

[Figure 7](#) shows the time-averaged quantities of the vorticity and the flow velocity for the REC and the SSC, which were obtained from the PIV measurements. The Reynolds number of the jet is $Re \approx 3200$. In [figure 7\(a,b\)](#) it can be seen that, close to the trailing edge of the orifice, the shear layer has a smaller diameter than the orifice. The reason for this is the flow separation after the leading edge of the orifice shaping the so-called *vena contracta*. This effect can be seen as well in Brokof *et al.* (2023). The vorticity was calculated from the velocity field using $\bar{\omega}_z = (\nabla \times \bar{\mathbf{u}}) \cdot \mathbf{e}_z$, where \mathbf{e}_z is the unit vector in the z -direction. Comparing the values of the time-averaged vorticity $\bar{\omega}_z$ of the REC and the SSC, it can be seen that, for the non-whistling case SSC, the values for $\bar{\omega}_z$ are locally more concentrated, while for the REC they are spread in the y -direction. This is caused by the strong coherent vortex shedding at the orifice, which is visible in [figure 1](#) as well. The same effect can be seen in the mean velocity in [figure 7\(c\)](#).

It is important to note that the both jets of the REC and the SSC are slightly asymmetric. The asymmetry for the REC is visible in the time-averaged axial velocity profile, while its time-averaged vorticity profile is more symmetric. For the SSC, the time-averaged velocity profile is more symmetric, while the time-averaged vorticity is more asymmetric.

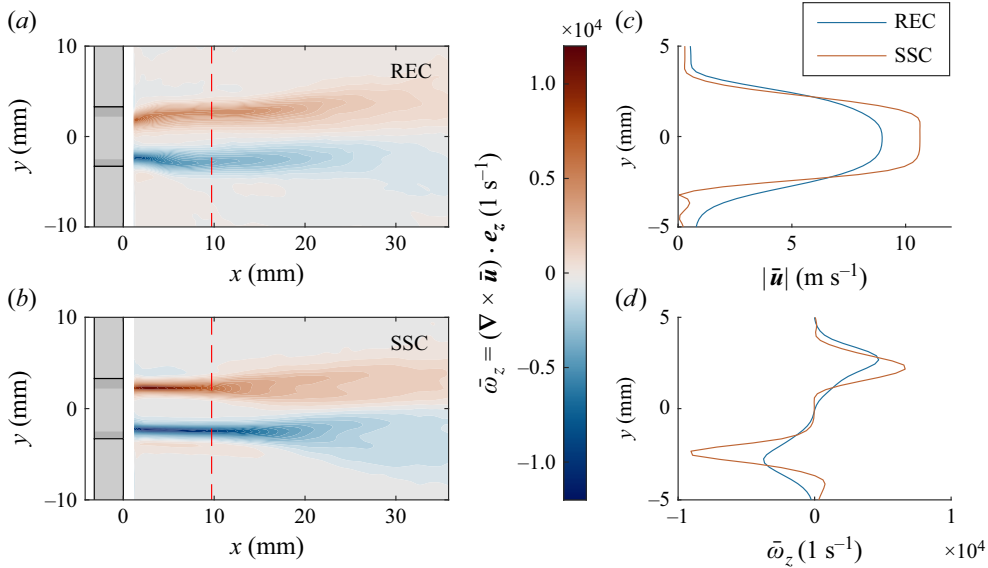


Figure 7. Time-averaged quantities from experimentally determined velocity fields for a mass flow rate of $\dot{m} = 0.3 \text{ g s}^{-1}$: (a,b) $\bar{\omega}$ fields for reference cavity (REC) and slow-sound cavity (SSC), (c) velocity profiles $|\bar{\mathbf{u}}|$ at $x = 10 \text{ mm}$ and (d) mean vorticity $\bar{\omega}$ at $x = 10 \text{ mm}$. The scientific colour map *vik* of Crameri, Shephard & Heron (2020) is used to prevent the exclusion of readers with colour-vision deficiencies.

This asymmetry in the flow might originate from the asymmetry of the geometry, where the cavities are placed along one of the corners of the waveguide to enable the PIV, or from a small leakage flow close to the wall due to imperfect sealing between the orifice plate and the duct sidewall.

The fluctuating vorticity ω_z is shown in figure 8. The instantaneous vorticity fields for the REC and the SSC are shown in figure 8(a,b), where every 8th vector of the velocity fluctuations \mathbf{u}' is plotted. For the REC, a clear pattern of alternating local extrema of the vorticity can be seen. They correspond to the coherent vortex shedding due to the whistling. Due to the pressure fluctuations in the resonating deep cavity, vortices are shed in regular intervals at the orifice and travel downstream. In figure 8(c) the patches of the vorticity passing $x = 10 \text{ mm}$ are plotted over time t . In this panel 7 periods are visible over a time of 10 ms, giving an approximate whistling frequency of 700 Hz. The actual whistling frequency of the system based on the pressure signal at the upstream microphone is in this case 688 Hz, which is noticeably larger than for the self-excited tests ($f = 661 \text{ Hz}$). This discrepancy might originate from a small leakage at the interface between the additively manufactured elements and the duct sidewall due to imperfect sealing. The slight asymmetry of the flow, which was discussed for figure 7, is visible in figure 8(a) as well. For a symmetric flow, a maximum of the vorticity on the upper half of the jet should coincide in space and time with a minimum of the vorticity on the lower half of the jet and *vice versa*.

For the SSC, the fluctuations of the vorticity are smaller. There is no visible periodic pattern neither in space nor in time. The absence of strong fluctuations in ω'_z shows that the system is not whistling. Both the vorticity ω'_z and the velocity oscillations \mathbf{u}' are smaller close to the orifice than for the whistling case (REC) because there are no acoustic oscillations forcing the jet at the orifice. Only at a larger distance x from the orifice do the values for \mathbf{u}' and ω'_z grow stronger, because of hydrodynamic Kelvin–Helmholtz instabilities of the turbulent jet.

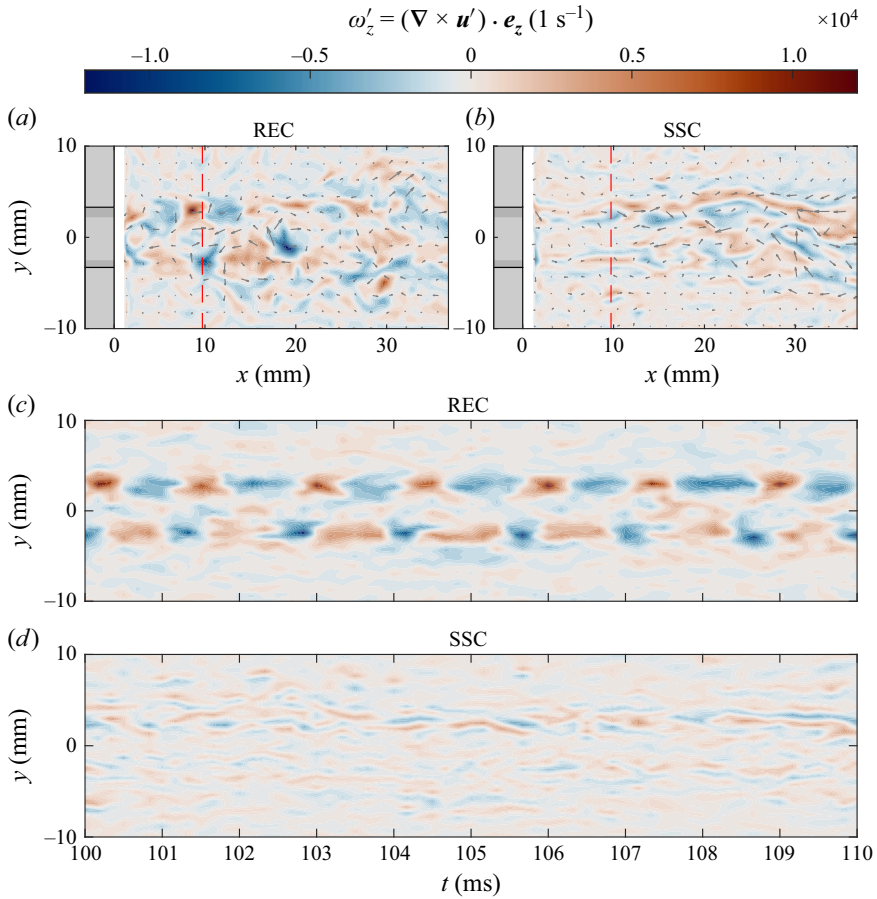


Figure 8. Vorticity fluctuations ω'_z from experimentally determined velocity fields: (a,b) instantaneous ω'_z fields for REC and SSC with fluctuating velocity \mathbf{u}' where every 8th vector of the available vector field is plotted, (c,d) ω'_z at $x = 10$ mm. Movies can be seen in supplementary material.

4.3. Vortex sound

In this section, the production of sound for the REC is discussed to obtain insight into the aeroacoustic mechanism leading to whistling. The set point for the mass flow rate is $\dot{m} = 0.3 \text{ g s}^{-1}$. The vortex sound theory from Howe (1975, 1980) is used to compute the acoustic energy production using a hybrid approach as in Boujo *et al.* (2020), where vortical velocity field from the PIV is used in conjunction with the potential velocity field obtained from the finite element method (FEM) which is used to solve the eigenvalue problem of the Helmholtz equation. This estimation of the narrow-band sound production from the self-oscillating aeroacoustic mode is achievable in the case of the whistling REC by using the phase-averaged PIV data, as these coherent oscillations clearly dominate the acoustic PSD (see figure 6), with its first harmonic being more than 30 dB weaker.

However, in the case of the SSC, one cannot estimate the overall noise intensity with this method because, in contrast to the REC, the PSD contains multiple resonance peaks energised by the broadband noise of the low Mach turbulent flow. One can for instance notice the quarter-wave resonance peak at 445 Hz which corresponds to the 660 Hz peak

in the case of the REC (with the slow-sound effect of $c/c_{eff} \approx 1.5$ from the addition of the small cavities).

The acoustic energy production from the interaction of an acoustic field with advected vorticity fluctuations in a low Mach flow can be expressed as (Howe 1980; Bruggeman *et al.* 1991; Boujo *et al.* 2020)

$$P = -\rho \widetilde{(\boldsymbol{\omega} \times \mathbf{u})} \cdot \mathbf{u}_{ac}. \quad (4.4)$$

This expression is the projection onto the acoustic velocity field \mathbf{u}_{ac} of the coherent component of the Lamb vector field $\boldsymbol{\omega} \times \mathbf{u}$. When multiplied by the fluid density ρ , $\boldsymbol{\omega} \times \mathbf{u}$ can be regarded as a force vector field similar to the Magnus force causing lift on a fluidic element (Bruggeman *et al.* 1991). This force exerts work on the acoustic medium. If this force vector is pointing in the opposite direction to the local acoustic velocity, sound is produced, otherwise it is dissipated. Integrating (4.4) over a volume gives the sound power produced or dissipated by vortices in this area. The reader is referred to Howe (1975) for a comprehensive derivation and discussion of the vortex sound mechanism, including practical examples.

To apply (4.4) to the problem of orifice whistling, the (irrotational) acoustic velocity field needs to be obtained. Theoretically, the irrotational velocity field can be separated from the solenoidal velocity field using a Helmholtz decomposition. This was done for example in Ho & Kim (2021) for the case of deep cavity whistling or by Matsuura & Nakano (2012) for the case of hole tone whistling. However, this Helmholtz decomposition requires knowledge about the boundaries. Due to the restricted field of view and scattered light close to the orifice, values for the velocity close to the boundaries are not obtained by the PIV measurements. Therefore, the Helmholtz decomposition cannot be applied in the present case. Instead, the acoustic velocity is obtained using a FEM model to solve the eigenvalue problem of the Helmholtz equation. This method was already successfully applied by Boujo *et al.* (2020) for the case of a Helmholtz resonator with grazing flow. The Comsol Multiphysics 5.6 pressure acoustics module is used for this study.

A cut view of the (x, y) -plane of the three-dimensional FEM model, going through the centre of the orifice at $z = 0$, is shown in figure 9(a). The model consists of an upstream domain, the orifice, the REC and a semi-spherical downstream domain with a radius of 100 mm. On the upstream side, the boundary Γ_u is modelled as an impedance boundary. The value for the impedance was taken from impedance measurements at a forcing frequency of $f = 670$ Hz, see Appendix B. The downstream boundary Γ_d is modelled as non-reflecting for spherical waves. All other boundaries are modelled as sound-hard walls. Losses apart of the boundaries Γ_u and Γ_d are not modelled. For the real-world system, thermoviscous losses and losses associated with the mean flow at the orifice will affect the reflection of waves there and therefore also the resonance frequencies. These effects are neglected for this FEM study. The eigenvalues are determined using the ARPACK implementation of Comsol Multiphysics. The determined eigenfrequency closest to the whistling frequencies of figure 6 is $f = 671.2 - 3.36i$. The pressure field p_{ac} in figure 9(a) shows a large amplitude acoustic pressure close to the downstream side of the orifice, similar to a quarter-wave mode. The acoustic velocity field is complex. The section corresponding to the region of interest of the PIV data with the same grid points is shown in figure 9(b). Note, that the real and imaginary vectors are scaled by different amounts for this figure. At the orifice, the absolute value of the imaginary part of the velocity is a factor 4 larger than the real part. The largest values for \mathbf{u}_{ac} are in proximity to the orifice.

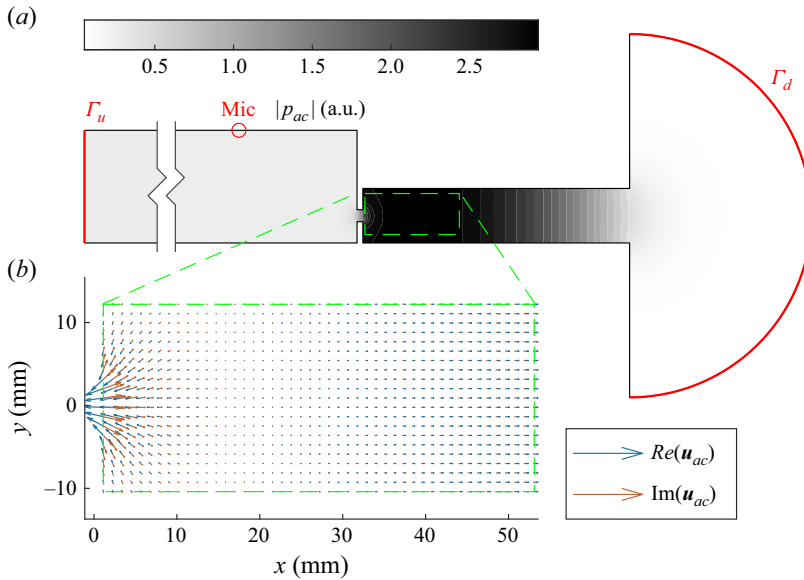


Figure 9. (a) Cut view of absolute acoustic pressure field $|p_{ac}|$ at eigenfrequency of $f = 671.2 - 3.36i$ Hz obtained using the FEM for the Helmholtz equations, with a non-reflective boundary Γ_d and an impedance boundary Γ_u . (b) complex vector field of acoustic velocity \mathbf{u}_{ac} , where every 5th vector is plotted.

The acoustic velocity field obtained from the FEM simulation is phase locked with the PIV velocity field using the pressure recorded at the microphone at $x = -68.2$ mm and the corresponding acoustic pressure from the FEM simulation. By dividing the band-pass-filtered Hilbert transform of the measured pressure signal p_m by the complex pressure from the FEM at this location, a non-dimensional complex time-dependent factor is obtained, which can be applied to scale the complex acoustic velocity field for the appropriate phase locking. The pressure downstream of the orifice p_d can be obtained accordingly. The respective real parts yield the instantaneous pressures and velocities. All relevant quantities, like the PIV and FEM velocity fields, can be phase averaged using the phase ϕ of the Hilbert transformed pressure p_d , which is then of the form $\tilde{p}_d = |p_d| \cos(\phi)$. The phase-averaged pressures and velocities at the downstream side of the orifice are shown in [figure 10](#) as a function of the phase ϕ . [Figure 10\(a\)](#) shows the pressure fluctuations at the orifice \tilde{p}_d and at the microphone location \tilde{p}_m , as well as the components in the x -direction of the acoustic velocity \mathbf{u}_{ac} and the coherent velocity fluctuations $\tilde{\mathbf{u}}$ at $x = 1.13$ mm spatially averaged over the outlet with the diameter D , expressed by the integral $1/D \int_0^D \tilde{u}_x dy$, which is evaluated using the trapezoidal rule. It can be seen clearly that \mathbf{u}_{ac} is shifted to \tilde{p}_d by $\Delta\phi = 270^\circ$. Note that the velocity is defined in the positive x -direction. The average axial velocity, which is proportional to the mass flow oscillations through the orifice, has its maximum slightly earlier at $\Delta\phi = 255^\circ$, i.e. the spatially averaged acoustic velocity is roughly in phase with the spatially averaged axial velocity fluctuations. This is a necessary condition due to the continuity equation (Gerrard [1971](#)). [Figure 10\(b,c\)](#) shows the axial velocity components before averaging. [Figure 10\(b\)](#) shows that \tilde{u}_x close to the edge of the orifice at $y = \pm 2$ mm leads \tilde{u}_x at the centre of the jet at $y = 0$ mm. This behaviour is typical for pulsatile flows with a finite viscosity (Shemer, Wygnanski & Kit [1985](#)).

With the phase-locked velocity field from the PIV and the acoustic velocity field from the FEM, the local sound production and dissipation P can be calculated using (4.4).

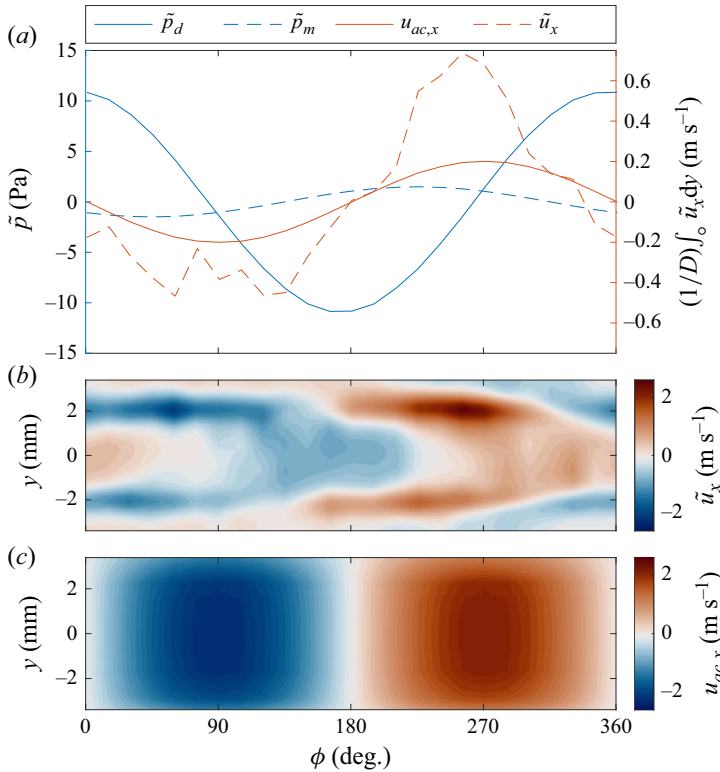


Figure 10. Phase-averaged pressure and velocity fluctuations downstream of the orifice, (a) acoustic pressure downstream of orifice \tilde{p}_d , acoustic pressure measured at the upstream microphone \tilde{p}_m and axial components of velocity fluctuations \tilde{u}_x and acoustic velocity $\tilde{u}_{ac,x}$ averaged spatially over the area of the orifice at $x = 1.1$ mm, (b) \tilde{u}_x at $x = 1.1$ mm, (c) $\tilde{u}_{ac,x}$ at $x = 1.1$ mm.

Phase averaging is employed to study P over one acoustic cycle. The results are shown in figure 11. Figure 11(a) shows a detail of the vortex sound production with the Lamb vectors $\boldsymbol{\omega} \times \mathbf{u}$ and the acoustic velocity vectors \mathbf{u}_{ac} at $\phi = 0^\circ$. Figure 11(b–e) shows the vortex sound production P for 4 bins with the edges $\phi = [0^\circ, 90^\circ, 180^\circ, 270^\circ, 360^\circ]$. The figure shows that sound is produced and dissipated predominantly in the shear layer close to the orifice, where both the vorticity ω_z and the acoustic velocity \mathbf{u}_{ac} are large. With distance to the orifice, \mathbf{u}_{ac} decays rapidly and thus also do the sound production and dissipation P . The area with the largest acoustic velocity and therefore with the largest contribution to sound production and dissipation is in the orifice, which is not resolved by the PIV. Figure 11(a) shows the interplay of the fluctuating Lamb vector $\boldsymbol{\omega} \times \mathbf{u}$ (red vectors) with the acoustic velocity \mathbf{u}_{ac} (blue vectors) for the phase $\phi = [0^\circ, 90^\circ]$. According to (4.4), sound is produced when their scalar product is negative with the vectors pointing in opposite directions, and it is dissipated when it is positive with the vectors pointing in the same direction. Over one acoustic cycle (figure 11b–e), the shed vortices are advected with the mean flow. The phase of the acoustic field determines if they produce or dissipate acoustic energy. In the first bin $\phi = [0^\circ, 90^\circ]$, the acoustic velocity is negative. The shed vortex ring produces sound close to the centre line and dissipates sound close to the trailing edge of the orifice. In the second bin $\phi = [90^\circ, 180^\circ]$ the counter-rotating vortex ring behind the first vortex ring dissipates acoustic energy, while the first travels further downstream and continues to produce acoustic energy. In the third bin $\phi = [180^\circ, 270^\circ]$,

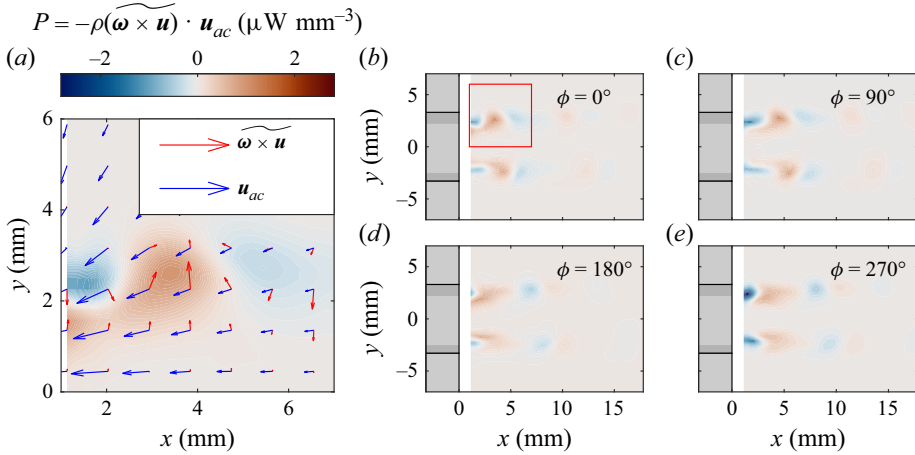


Figure 11. Phase-averaged vortex sound production P calculated using Howe's corollary: (b–e) for various phases ϕ , (a) detail of $\phi = 0^\circ$ with Lamb vectors $(\widetilde{\omega \times u})$ and acoustic velocity vectors u_{ac} , where every 4th vector is plotted. Movies can be seen in supplementary material.

the direction of the acoustic velocity reverses and thus the roles of the pair of vortex rings switch. The first vortex now dissipates acoustic energy, while the counter-rotating second vortex generates acoustic energy. However, due to the large distance of the first vortex ring to the orifice, it is in a range where the acoustic velocity is low. Therefore, less acoustic energy is dissipated by the first ring than generated by the counter-rotating second ring. In the fourth bin $\phi = [270^\circ, 360^\circ]$, the largest dissipation of acoustic energy can be observed, when a new vortex ring emerges from the orifice while the acoustic velocity still points outwards in the streamwise direction. With the reversal of the acoustic velocity after $\phi = 360^\circ$, the cycle repeats and this vortex ring will generate acoustic energy.

The net sound production can be analysed by integrating P over one phase-averaged acoustic cycle of length $T = 1/f$. The resulting scalar field shows where, on average, sound is produced and where it is dissipated. The temporal integral of P is shown in figure 12(a). Overall, the absolute value of the sound production $|P|$ decays fast with distance to the orifice x . The reason for this is the strong decay of the acoustic velocity u_{ac} for increasing x , which can be seen in figure 9(b). Additionally, local maxima and minima can be observed in figure 12. They correspond to the travelling vortex rings in the oscillating acoustic field. Close to the trailing edge of the orifice, sound is predominately dissipated. The maximum of sound production is a little further downstream and closer to the centre of the jet. The local maxima and minima alternate in the streamwise x -direction. Integrating in the y -direction yields figure 12(b), where this alternating pattern can be seen more clearly. The integral $1/T \iiint P d\tau dy dx$ is positive, indicating that, in this part of the flow, more sound is produced than dissipated. It can be seen that for small x sound is mostly dissipated. Because the sound production is not at a local minimum there, it can be assumed to decrease further when approaching the trailing edge of the orifice. The integration of the temporal integral of P in the x -direction is shown in figure 12(c). There, it can be seen that sound is on average produced on the inside of the cylindrical vortex sheet. On the outside, sound is on average dissipated. In this plot, a slight asymmetry is visible as well, with more dissipation occurring for $y < 0$.

Assuming rotational symmetry of $1/T \int_0^T P d\tau dx$ about the x -axis, P can be integrated over the whole region observed by the PIV $(x, \theta, y) \in [1.13 \text{ mm}, 53 \text{ mm}] \times [0, 2\pi] \times [0 \text{ mm}, 12 \text{ mm}]$, yielding a sound power of approximately $5.2 \mu\text{W}$.

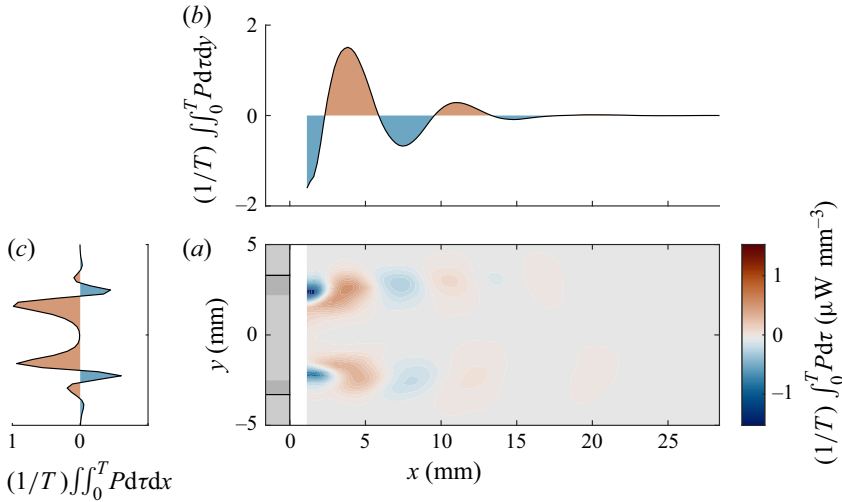


Figure 12. (a) Temporal integration of vortex sound production P , (b,c) spatial integration in the y - and x -directions.

This produced sound power can be compared with the radiated sound power in the upstream duct. Assuming plane wave propagation and no reflections at the inlet, the sound power radiated in a duct is (Munjal 2014)

$$A \frac{1}{T} \overline{p_{ac} v_{ac}} \approx A \frac{1}{2} \frac{\hat{p}_{ac}^2}{\rho c}, \quad (4.5)$$

where \hat{p}_{ac} is the Fourier coefficient of the pressure measured at the microphone location at the whistling frequency and A is the cross-sectional area of the duct. This calculation yields approximately $2.5 \mu\text{W}$ for the upstream side. The sound radiation on the downstream side was not measured directly, however, it can be assumed that it is of a similar order of magnitude. Therefore, it can be deduced that a significant portion of the net vortex sound production occurs outside of the orifice.

5. Conclusion

This paper demonstrates the suppression of an aeroacoustic instability using the slow-sound effect. The main cavity with a bias flow orifice is detuned, without altering its dimensions, such that the constructive feedback loop between the hydrodynamic shear layer mode and the acoustic mode is hindered. With this method, the instability is successfully suppressed and the self-oscillating aeroacoustic mode does not develop. In contrast to the classic passive control strategy based on damping enhancement at the instability frequency with the addition of dissipative resonators tuned around that frequency, we add small volumes that do not resonate at the instability frequency. In fact, their resonance frequency is significantly higher, and they simply behave like acoustic compliances. In their low-frequency range, they soften the impedance of the wall of the main cavity and move its eigenfrequencies away from the frequency range where the orifice with bias flow exhibits an acoustic energy amplification potential. This change of eigenfrequency is induced by the so-called ‘slow-sound’ effect because it can be interpreted as a change in the effective speed of sound in the main cavity. It enables a detuning of the main cavity from the frequency range where the orifice amplifies incident waves, in order to hinder the emergence of the aeroacoustic instability. For the whistling

reference cavity, the sound produced and dissipated by the unsteady vorticity at the orifice is calculated with Howe's energy corollary, using a hybrid approach that combines PIV data and the irrotational velocity field obtained from finite element simulations of the Helmholtz equation. This method provides information on the spatio-temporal distribution of the sound sources and sinks from the unsteady jet. To the best of the authors' knowledge, this is the first reporting of the sound production map of the whistling of a bias flow orifice connected to a deep cavity based on experimental data. The estimated sound radiation from the field of view is in agreement with the sound production measured in the upstream duct. In conclusion, if the frequency of one of the jet's hydrodynamic modes is close to the frequency of an acoustic resonance, whistling can occur. By preventing these frequencies to match, as it is achieved with the SSC, the whistling is effectively mitigated.

Supplementary movies. Supplementary movies are available at <https://doi.org/10.1017/jfm.2025.10569>.

Funding. This research is part of the TORCH project and financed by the European Research Council (ERC) (grant number 820091).

Declaration of interests. The authors declare that they have no competing interests that would have had any influence on the results presented in this paper.

Author contributions. R.M. and K.P. performed the experimental investigations. R.M. designed the acoustic specimens and processed the experimental data. All authors discussed the results. N.N. and R.M. conceptualised the study. N.N. supervised the research. R.M. and N.N. wrote the manuscript. All authors reviewed and approved the final version of the article.

Appendix A. Low-frequency limit of the dispersion relation

The following derivation of the low-frequency limit of the dispersion relation shows how the effective speed of sound is reduced in the low-frequency limit. The reader is referred to Munjal (2014) for a detailed derivation of the dispersion relation for the general case of rectangular ducts with locally reacting lining.

By adding sidewall small cavities to the main deep cavity downstream of the orifice, the wavenumbers in the y and in z directions change and therefore also affect the axial wavenumber k_x . Exploiting the symmetry of the system about the x -axis, the compatibility relation of modes in a rectangular duct can be written as

$$k^2 = k_x^2 + k_y^2 + k_z^2 = k_x^2 + 2k_y^2. \quad (\text{A1})$$

Therefore, only an expression for dispersion in the y -direction needs to be derived. For convenience, a new coordinate system is introduced, where $y=0$ is the position of the hard wall and $y=h$ is the position of the wall with sidewall small cavities. The boundary condition at $y=0$ is $-u_y/p=0$ and $p/u_y=Z_w$ at $y=h$, where Z_w is the sidewall impedance.

Using the boundary conditions and the solutions to the wave equation for p and u , one can derive the following dispersion relation in the y -direction (Munjal 2014):

$$\tan(k_y h) = -i \frac{\rho c}{Z_w} \frac{k}{k_y}, \quad (\text{A2})$$

where the wall impedance Z_w can be approximated in the low-frequency limit by the compliance $Z_{w,lf} = ia_n/(V_r k \Phi)$ with the volume of the small cavities V_r , and $\Phi = a_n/(h \Delta L)$ is the porosity of the wall, where ΔL is the length of one section of the deep cavity corresponding to one small cavity. Plugging this expression into (A2), leads to

$$\frac{k_{x,lf}}{k} = \sqrt{1 + \frac{2\Phi V_r}{a_n h}}. \quad (\text{A3})$$

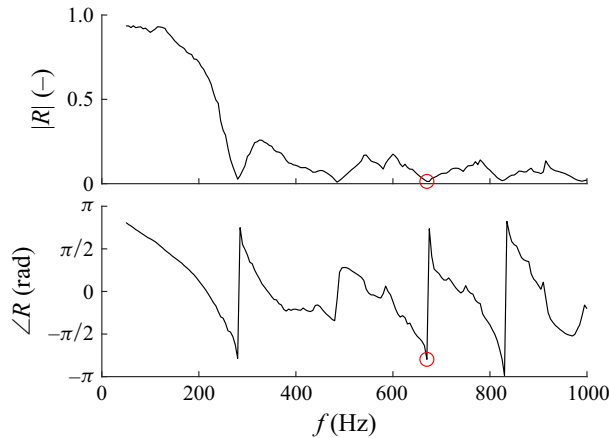


Figure 13. Reflection coefficient R of boundary to near-anechoic end $x = -393.2$ mm, the red circle marks the values at $f = 670$ Hz taken for the FEM model.

By using the expression for the wall porosity $\Phi = a_n/(h\Delta L)$, we arrive at the general expression $k_{x,l}/k = \sqrt{1 + V_c^{-1} \sum V_r}$ which is independent of the shape of the main cavity cross-section and small cavities, cf. Sugimoto & Horioka (1995).

Appendix B. Inlet impedance

To accurately model the upstream boundary, its impedance is measured using the multiple microphone method. The measurements are conducted without a mean flow because the flow velocity is negligible in the large cross-section of the near-anechoic termination. The results of the measurements are depicted in figure 13.

It can be seen that, below 280 Hz, the inlet boundary is mostly reflective. This can lead to resonances on the upstream side of the cavity in this frequency range. Above 280 Hz, the reflection coefficient is comparably low at around $R = 0.1$. For the whistling frequency of approximately $f = 670$ Hz, the reflection coefficient is $R < 0.05$. Thus, the resonance of the cavity plays the dominant role in the whistling mechanism.

REFERENCES

- ANDERSON, A.B.C. 1952 Dependence of *Pfeifenton* (Pipe tone) frequency on pipe length, orifice diameter, and gas discharge pressure. *J. Acoust. Soc. Am.* **24** (6), 675–681.
- ANDERSON, A.B.C. 1955 Structure and velocity of the periodic vortex-ring flow pattern of a *Primary Pfeifenton* (Pipe tone) jet. *J. Acoust. Soc. Am.* **27** (6), 1048–1053.
- ARMBRUSTER, W., HARDI, J. & OSCHWALD, M. 2022 Impact of shear-coaxial injector hydrodynamics on high-frequency combustion instabilities in a representative cryogenic rocket engine. *Intl J. Spray Combust. Dyn.* **14** (1–2), 118–130.
- AURÉGAN, Y. & PAGNEUX, V. 2015 Slow sound in lined flow ducts. *J. Acoust. Soc. Am.* **138** (2), 605–613.
- AURÉGAN, Y. & STAROBINSKI, R. 1999 Determination of acoustical energy dissipation/production potentiality from the acoustical transfer functions of a multiport. *Acta Acust. United with Acust.* **85** (6), 788–792.
- BLAKE, W.K. & POWELL, A. 1986 The development of contemporary views of flow-tone generation. In *Recent Advances in Aeroacoustics*, (eds. A. Krothapalli & C.A. Smith), pp. 247–325. Springer New York.
- BOUJO, E., BOURQUARD, C., XIONG, Y. & NOIRAY, N. 2020 Processing time-series of randomly forced self-oscillators: the example of beer bottle whistling. *J. Sound Vib.* **464**, 114981.
- BOURQUARD, C., FAURE-BEAULIEU, A. & NOIRAY, N. 2021 Whistling of deep cavities subject to turbulent grazing flow: intermittently unstable aeroacoustic feedback. *J. Fluid Mech.* **909**, A19.
- BRANDÃO, R. & SCHNITZER, O. 2020 Acoustic impedance of a cylindrical orifice. *J. Fluid Mech.* **892**, A7.

- BROKOF, P., GUZMÁN-IÑIGO, J., YANG, D. & MORGANS, A.S. 2023 The acoustics of short circular holes with reattached bias flow. *J. Sound Vib.* **546**, 117435.
- BRUGGEMAN, J.C., HIRSCHBERG, A., VAN DONGEN, M.E.H., WIJNANDS, A.P.J. & GORTER, J. 1991 Self-sustained aero-acoustic pulsations in gas transport systems: experimental study of the influence of closed side branches. *J. Sound Vib.* **150** (3), 371–393.
- CRAMERI, F., SHEPHARD, G.E. & HERON, P.J. 2020 The misuse of colour in science communication. *Nat. Commun.* **11** (1), 5444.
- CUMMER, S.A., CHRISTENSEN, J. & ALÙ, A. 2016 Controlling sound with acoustic metamaterials. *Nat. Rev. Mater.* **1** (3), 16001.
- GERRARD, J.H. 1971 An experimental investigation of pulsating turbulent water flow in a tube. *J. Fluid Mech.* **46** (1), 43–64.
- GUZMÁN-IÑIGO, J. & MORGANS, A.S. 2024 Designing the edges of holes (with bias flow) to maximise acoustic damping. *J. Sound Vib.* **575**, 118224.
- HO, Y.W. & KIM, J.W. 2021 A wall-resolved large-eddy simulation of deep cavity flow in acoustic resonance. *J. Fluid Mech.* **917**, A17.
- HOWE, M.S. 1980 The dissipation of sound at an edge. *J. Sound Vib.* **70** (3), 407–411.
- HOWE, M.S. 1975 Contributions to the theory of aerodynamic sound, with application to excess jet noise and the theory of the flute. *J. Fluid Mech.* **71** (4), 625–673.
- HUSSAIN, A.K.M.F. & REYNOLDS, W.C. 1970 The mechanics of an organized wave in turbulent shear flow. *J. Fluid Mech.* **41** (2), 241–258.
- JANG, S.-H. & IH, J.-G. 1998 On the multiple microphone method for measuring in-duct acoustic properties in the presence of mean flow. *J. Acoust. Soc. Am.* **103** (3), 1520–1526.
- JIMÉNEZ, N., ROMERO-GARCÍA, V., PAGNEUX, V. & GROBY, J.-P. 2017 Quasiperfect absorption by subwavelength acoustic panels in transmission using accumulation of resonances due to slow sound. *Phys. Rev. B* **95** (1), 014205.
- KIERKEGAARD, A., ALLAM, S., EFRAIMSSON, G. & ÅBOM, M. 2012 Simulations of whistling and the whistling potentiality of an in-duct orifice with linear aeroacoustics. *J. Sound Vib.* **331** (5), 1084–1096.
- LEE, K., LEE, S., LEE, S. & CHEONG, C. 2022 Numerical investigation of whistling sound in narrow-gap flow of automobile side mirror. *Appl. Acoust.* **197**, 108893.
- MA, R., SLABOCH, P.E. & MORRIS, S.C. 2009 Fluid mechanics of the flow-excited Helmholtz resonator. *J. Fluid Mech.* **623**, 1–26.
- MATSUURA, K. & NAKANO, M. 2012 A throttling mechanism sustaining a hole tone feedback system at very low Mach numbers. *J. Fluid Mech.* **710**, 569–605.
- MINIERO, L., MENSAH, G.A., BOURQUARD, C. & NOIRAY, N. 2023 Failure of thermoacoustic instability control due to periodic hot gas ingestion in Helmholtz dampers. *J. Sound Vib.* **548**, 117544.
- MUNJAL, M.L. 2014 *Acoustics of Ducts and Mufflers*, 2nd edn. Wiley.
- RADOSZ, J. 2021 Effects of tonal noise on workers' annoyance and performance. *Noise Health* **23** (111), 117.
- RUSSO, S., FABRE, D., GIANNETTI, F. & LUCHINI, P. 2016 The speed of sound in periodic ducts. *J. Sound Vib.* **361**, 243–250.
- SHEMER, L., WYGNANSKI, I. & KIT, E. 1985 Pulsating flow in a pipe. *J. Fluid Mech.* **153**, 313.
- SIERRA-AUSIN, J., FABRE, D., CITRO, V. & GIANNETTI, F. 2022 Acoustic instability prediction of the flow through a circular aperture in a thick plate via an impedance criterion. *J. Fluid Mech.* **943**, A48.
- SONDHAUS, C. 1854 Ueber die beim Ausströmen der Luft entstehenden Töne. *Ann. Phys.* **167** (1), 126–147.
- STRUTT, J.W. 1945 *The Theory of Sound*. Dover Books on Physics, vol. 2, Dover Publications.
- SUGIMOTO, N. & HORIOKA, T. 1995 Dispersion characteristics of sound waves in a tunnel with an array of Helmholtz resonators. *J. Acoust. Soc. Am.* **97** (3), 1446–1459.
- TESTUD, P., AURÉGAN, Y., MOUSSOU, P. & HIRSCHBERG, A. 2009 The whistling potentiality of an orifice in a confined flow using an energetic criterion. *J. Sound Vib.* **325** (4–5), 769–780.
- THEAKSTON, F. 2011 *Burden of Disease From Environmental Noise: Quantification of Healthy Life Years Lost in Europe*. World Health Organization, Regional Office for Europe.
- UNNIKRISHNAN, S. & GAITONDE, D.V. 2016 Acoustic, hydrodynamic and thermal modes in a supersonic cold jet. *J. Fluid Mech.* **800**, 387–432.
- YANG, D. & MORGANS, A.S. 2016 A semi-analytical model for the acoustic impedance of finite length circular holes with mean flow. *J. Sound Vib.* **384**, 294–311.
- YANG, D. & MORGANS, A.S. 2017 The acoustics of short circular holes opening to confined and unconfined spaces. *J. Sound Vib.* **393**, 41–61.
- ZHANG, Q. & BODONY, D.J. 2012 Numerical investigation and modelling of acoustically excited flow through a circular orifice backed by a hexagonal cavity. *J. Fluid Mech.* **693**, 367–401.